PHYSICAL REVIEW MATERIALS **00**, 004000 (2025)

Cleavable quaternary oxychlorides with high magnetic ordering temperatures

Andrew F. May [1,*] George Yumnam [1] Raphael P. Hermann [1] Stuart Calder [2] Benjamin M. Lefler [3] Steven J. May [3] Zachary E. Brubaker [4] Matthew Brahlek [1] Xiaodong Xu,[5] Dmitry Ovchinnikov,[5,6] and Michael A. McGuire [1]

[1]*Materials Science and Technology Division, Oak Ridge National Laboratory, Oak Ridge, Tennessee 37831, USA*

[2]*Neutron Scattering Division, Oak Ridge National Laboratory, Oak Ridge, Tennessee 37831, USA*

[3]*Department of Materials Science and Engineering, Drexel University, Philadelphia, Pennsylvania 19014, USA*

[4]*Nuclear Nonproliferation Division, Oak Ridge National Laboratory, Oak Ridge, Tennessee 37831, USA*

[5]*Department of Physics and Department of Materials Science and Engineering, University of Washington, Seattle, Washington 98195, USA*

[6]*Department of Physics and Astronomy, University of Kansas, Lawrence, Kansas 66045, USA*

(Received 11 February 2025; accepted 13 March 2025; published xxxxxxxxxx)

Quaternary oxychlorides derived from Ruddlesden–Popper 3*d* transition metal oxides offer a route to cleavable crystals with bulk antiferromagnetic ordering temperatures reaching at least 550 K. Here, we study the magnetic, optical, and mechanical behavior of Sr_2FeO_3Cl, Ca_2FeO_3Cl, $Ca_3Fe_2O_5Cl_2$, and $Sr_3Fe_2O_5Cl_2$. Through optical absorption measurements, we show that these antiferromagnetic semiconductors have optical band gaps of ≈2.1(1) eV. The magnetic ordering symmetries and temperatures were probed by neutron powder diffraction and Mössbauer spectroscopy on polycrystalline samples, demonstrating Néel temperatures (T_N) near room temperature in the single layer Sr_2FeO_3Cl ($T_N \approx 311$ K) and Ca_2FeO_3Cl ($T_N \approx 360$ K), and the double-layer compound $Sr_3Fe_2O_5Cl_2$ ~~ordering near~~ $T_N \approx 545$ K. The high-spin moments of Fe^{3+} lie within the basal plane and the magnetic structures are compensated within each magnetic layer and characterized by magnetic propagation vectors $\boldsymbol{k} = (\frac{1}{2}\frac{1}{2}0)$. Magnetization results demonstrate the quasi-2D nature of the magnetism, with a broad maximum in the susceptibility near $2T_N$ for Sr_2FeO_3Cl. Scotch tape tests and mechanical exfoliation onto SiO_2 confirm the micaceous nature of these crystals with cleavage down to a single unit cell (two magnetic layers) achieved for $Sr_3Fe_2O_5Cl_2$. This paper highlights strong antiferromagnetic interactions, semiconducting band gaps, and cleavability of quaternary Fe-based oxychlorides and motivates future work on crystals and exfoliated flakes of these and related oxyhalide systems.

DOI: 10.1103/PhysRevMaterials.00.004000

I. INTRODUCTION

The scientific impact that resulted from exfoliation-based studies of layered van der Waals (vdW) materials has been immense. A wide variety of condensed matter topics have been influenced or emerged, such as optoelectronic-valley effects in transition metal dichalcogenides, the emergence of correlations and superconductivity in twisted or ~~Moire~~ superstructures, and spin-based functionality in vdW heterostructures [1–12]. Each subfield exploring the physics of cleavable materials has a different property that makes a bulk crystal especially appealing, such as a low defect concentration or a high carrier mobility. For magnetic materials, high ordering temperatures are paramount in the pursuit of room-temperature functionality that might be exploited for information technologies. Efforts to utilize antiferromagnetic materials continue to increase owing to their potential for fast dynamics, robustness against magnetic fields, the fact that they do not produce large stray fields, and because they can possess strong magnetotransport effects [13–16]. As such, antiferromagnetic vdW materials with high Néel temperatures (T_N) may become particularly interesting.

Transition metal oxyhalides can form layered vdW structures containing large magnetic moments that order at high temperatures. This study focuses on examples containing high-spin Fe^{3+} ($S = \frac{5}{2}$). The materials can be viewed as derived from Ruddlesden–Popper oxides such as $Sr_3Fe_2O_7$ (or Sr_2FeO_4), as illustrated in Fig. 1. In the double-layer compound $Sr_3Fe_2O_7$, a nominal valence of Fe^{4+} results in a charge disproportionation transition at 340 K; subsequent antiferromagnetic ordering occurs below $T_N = 115$ K [17,18]. The nominal valence of Fe^{4+} is relatively unstable and oxygen vacancies can easily form and modify the magnetism [17,19]. The material can be reduced to $Sr_3Fe_2O_6$, where only Fe^{3+} is present and this results in $T_N \approx 550$ K [17], although even small amounts of additional oxygen can significantly reduce the magnetic ordering temperature [18,19]. The Fe^{3+} oxidation state is also achieved by replacing two oxygen ions in $Sr_3Fe_2O_7$ by chlorine ions to form $Sr_3Fe_2O_5Cl_2$ [20,21]; the resulting Néel temperature is between 550–600 K [22].

The chemical reduction of $Sr_3Fe_2O_7$ to $Sr_3Fe_2O_5Cl_2$ occurs in an ordered manner, resulting in the formation of a vdW gap between chlorine ions that reside at the apical position of FeO_5Cl octahedra [20,21]. The octahedra are heavily distorted with Fe shifted toward the FeO_5 square pyramid and the strong magnetic interactions occur via superexchange through corner shared oxygen. A similar local environment is found in the

*Contact author: mayaf@ornl.gov

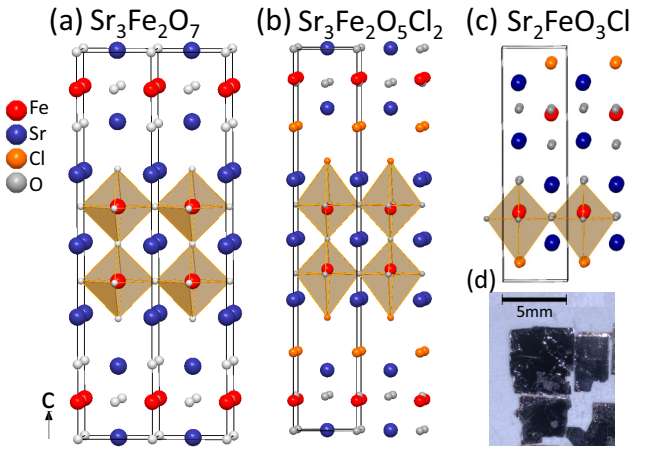

FIG. 1. Comparison of crystal structures for (a) double-layer Ruddlesden–Popper phase $Sr_3Fe_2O_7$, (b) double-layer $Sr_3Fe_2O_5Cl_2$, and (c) single-layer compound Sr_2FeO_3Cl. (d) Picture of thick $Sr_3Fe_2O_5Cl_2$ crystals.

single-layer Sr_2FeO_3Cl. As shown in Fig. 1, the double-layer compounds like $Sr_3Fe_2O_5Cl_2$ have a thicker magnetic block than the single-layer compounds like Sr_2FeO_3Cl, which have isolated Fe square nets. This leads to larger T_N values for the double-layer compounds; Sr_2FeO_3Cl is speculated to possess T_N slightly above ambient temperature [23]. Isostructural compounds are formed in the calcium systems, but barium-based oxychlorides often adopt other structure types or do not form. For instance, $Ba_3Fe_2O_5Cl_2$ forms in a chiral cubic structure and exhibits a coupling of magnetism and electric polarization [24,25]. Quaternary oxyhalides containing transition metals appear to be a large family of vdW magnetic materials that have not been considered much since the onset of exfoliation-based studies.

In this paper, we revisit the synthesis and properties of $Sr_3Fe_2O_5Cl_2$, $Ca_3Fe_2O_5Cl_2$, Ca_2FeO_3Cl, and Sr_2FeO_3Cl. We utilize polycrystalline samples for Mössbauer spectroscopy measurements to determine the magnetic ordering temperature and neutron powder diffraction to inspect sample quality and revisit the previously reported magnetic structures. All compounds have long-range order above room temperature and possess antiferromagnetic structures with moments oriented perpendicular to [001] and compensated within each magnetic layer. We report magnetization data for polycrystalline Sr_2FeO_3Cl, which demonstrate a Néel temperature near 310 K. In addition, a broad maximum of the magnetic susceptibility is observed near $2T_N$, demonstrating the significant short range order associated with the quasi-2D magnetism. Optical absorption measurements were used to characterize the band gaps, which are all near 2.1(1) eV. Finally, initial exfoliation trials coupled with atomic force microscopy have revealed that the $Sr_3Fe_2O_5Cl_2$ crystals can be exfoliated to a thickness of one unit cell.

II. METHODS

Crystals of $Sr_3Fe_2O_5Cl_2$, $Ca_3Fe_2O_5Cl_2$, and Ca_2FeO_3Cl were grown from molten $SrCl_2$ or $CaCl_2$ based on motivation from Ref. [21]. For all compositions grown, the crystals were plate-shaped with a typical lateral dimension of 1–10 mm; examples are shown in Fig. 1(d). The growths were performed in Pt crucibles with Pt lids, with crucibles sitting in box furnaces. Growth of phase pure Sr_2FeO_3Cl was not accomplished, although the phase was detected as an intergrowth with $Sr_3Fe_2O_5Cl_2$ in some growth products. Further refinement of the growth conditions should produce crystals of Sr_2FeO_3Cl based our observations and prior literature.

Representative growth details are as follows. $Sr_3Fe_2O_5Cl_2$ was grown using the nominal composition $39.6SrCl_2$-$Fe_2O_3 - 3SrCO_3$ with a homogenization at 1075 °C for 24 h followed by cooling to 850 °C at 1 °/h. $Sr_3Fe_2O_5Cl_2$ was also grown using the nominal composition $61.3SrCl_2$-$Fe_2O_3 - 4.01SrCO_3$ by cooling from 1100 °C to 920 °C at 1 °/h. $Ca_3Fe_2O_5Cl_2$ was grown using the nominal composition $50.2CaCl_2$-Fe_2O_3-$2CaCO_3$ with a homogenization at 1000 °C for 24 h followed by cooling to 750 °C at 2 °/h. Ca_2FeO_3Cl was grown using the nominal composition $73.7CaCl_2$-$Fe_2O_3 - 3CaCO_3$ with a homogenization at 950 °C for 36 h followed by cooling to 775 °C at 1 °/h. For the Ca-based materials, $Ca_2Fe_2O_5$ is a competing phase that was observed particularly when the $CaCl_2$ was mostly evaporated. Other conditions similar to these also produce oxychloride crystals and variations in rates/temperatures/compositions appear to impact the range of products and their quality from growth. Because of the similarity of the different phases that can form, a systematic optimization of the crystal growth would be beneficial. For instance, growth of pure Sr_2IrO_4 single crystals that are free of $Sr_3Ir_2O_7$ intergrowth/impurity benefits from a short dwell at high T where detrimental ~~evaporated~~ losses occur [26]. These oxychlorides are kept at lower temperatures than the iridate example, but the point is that many factors can influence the growth of such materials and an optimization has not been undertaken.

Polycrystalline samples were made in sealed, evacuated SiO_2 tubes utilizing CaO or SrO, ultradry $CaCl_2$ or $SrCl_2$ and Fe_2O_3 that were ground and loaded in an inert atmosphere glovebox to avoid moisture prior to the reaction. The reactions were heated at 800 °C for several days with intermediate grinding. A single-phase polycrystalline sample of $Ca_3Fe_2O_5Cl_2$ was not produced and thus Mössbauer spectroscopy and neutron diffraction data for that composition are not reported. The data are meant to provide representative information to spur and guide future research and are thus not meant to be all-inclusive for each composition.

High-purity starting materials were used with the lowest purity being ACS grade $SrCl_2 - 6H_2O$ (Alfa Aesar 33393) as the source of $SrCl_2$ for some flux growths. We typically have better success in crystal growth when starting with anhydrous chlorides but we also used dried hydrated sources. The following purity was used: $SrCO_3$, 99.994%; Fe_2O_3, 99.99%; $SrCl_2$, 99.995; CaO, 99.95%; $CaCO_3$, 99.99%; $CaCl_2$, 99.9%.

Neutron diffraction experiments were performed at beamline HB-2A at the High Flux Isotope Reactor at Oak Ridge National Laboratory. Samples of approximate mass 4 g or larger were sealed in 8-mm-diameter vanadium cans under helium atmosphere. The wavelength used was 2.41 Å. Measurements for Sr_2FeO_3Cl and Ca_2FeO_3Cl were performed at temperatures of 300 K and 4 K using a closed cycle

refrigerator. $Sr_3Fe_2O_5Cl_2$ was measured at room temperature. Refinements were performed using the program FullProf [27]. Magnetic refinements and symmetry allowed magnetic structures to be determined using SARAh [28] and the Bilbao Crystallographic Server [29]. The refined magnetic structure files (mcif) are available in the Supplemental Material (SM) [30].

Spectroscopic ellipsometry was carried out on the oxychloride crystals using a J. A. Woollam M2000-U instrument with incident light 65−75° from the surface plane of the [001]-oriented crystals. Measurements were made in ambient conditions at room temperature. The energy dependence of the refractive index (n) and extinction coefficient (k) were obtained through analysis performed with the CompleteEase software package. From k and the photon wavelength (λ), the optical absorption (α) was calculated using $\alpha = 4\pi k/\lambda$.

Mössbauer spectra were recorded using a Wissel GmbH constant acceleration drive calibrated with α-iron at room temperature, which also serves as an isomer shift reference. A 5 mCi ^{57}Co@Rh source was utilized. Initial room-temperature measurements used a NaI:Tl scintillator (Ritverc-2). Measurements in the Wissel MBF-1100 furnace between 295 and 570 K used a krypton gas proportional counter, with smaller maximum count rate but better signal-to-noise ratio. The source to detector distance is 16 cm when the furnace is used. The samples were pressed into 16-mm-diameter pellets, for instance using 300-mg boron nitride and 66 mg/cm^2 of sample for the $Sr_3Fe_2O_5Cl_2$ powder. Pellets were wrapped in one layer of aluminum foil to ensure good thermal contact and placed in a hollow-cylinder sample holder made of nickel, which contacted the thermocouple used for temperature regulation. We estimate a furnace temperature accuracy of better than 3%, i.e., 10–15 K. The furnace was dynamically pumped to <0.1 mBar residual pressure before and during heating. Measurements below room temperature were carried out using a Janis SHI-850 closed cycle cryostat and NaI:Tl scintillator. The temperature accuracy is on the order of 1 K.

Magnetization measurements were performed using two different instruments produced by Quantum Design. DC magnetization measurements were performed in a Magnetic Property Measurement System (MPMSXL) with an oven insert enabling measurements to 700 K. For the measurements in the MPMSXL, the sample was sealed in a quartz tube with a small amount of helium exchange gas. The data from the oven were scaled by 2.2% to match the low-T data near 310 K, which is within a reasonable error bar for the different configurations. A vibrating sample magnetometer (VSM) option was used in a Physical Property Measurement System to enable measurement to higher magnetic fields than are available in the MPMSXL. For the VSM measurements, single crystals were affixed to quartz paddles using GE varnish and measurements were performed to 130 kOe.

The neutron diffraction data, Mössbauer spectra, and optical absorption data are available online [31].

III. RESULTS AND DISCUSSION

A. Crystal and magnetic structure characterization

We utilized laboratory x-ray diffraction and neutron diffraction to probe the crystal and magnetic structures of polycrystalline samples that were produced via solid state reactions. ~~Because of the different c-axis lattice parameters, diffraction~~ scans off a crystal surface can easily differentiate the single-layer or double-layer crystals and thus this approach was utilized to isolate clean crystals where indications of a secondary phase were not present. The use of neutron diffraction is advantageous because neutron diffraction is sensitive to oxygen occupancy and directly probes the magnetic order. Firstly, we note that refinements did not detect off-stoichiometry in these materials and thus defects are anticipated to be present only in small concentrations. However, the selected neutron wavelength is better for probing the magnetism than the nuclear structures and dedicated structural studies could be beneficial. Tables of refined crystallographic parameters are provided within the SM [30]. We probed the crystal quality of $Sr_3Fe_2O_5Cl_2$ via single crystal x-ray diffraction and did not detect any evidence for significant stacking faults or phase intergrowth (see the SM [30]). These results suggest that the phases were formed as desired and the samples are of reasonable purity for investigations into their basic physical properties. These results are thus consistent with the expectation of site preference for O and Cl, which is based on prior literature and is necessary to produce the desired vdW gap. A similar site preference is also document for Sr_2FeO_3F [32].

Our Mössbauer spectroscopy experiments evidenced a small difference in the hyperfine fields when comparing single crystals to their polycrystalline counterparts. This may indicate that different defects (or concentrations thereof) form as a consequence of different synthesis approaches. The results are discussed in more detail below.

Neutron diffraction data at 300 K are shown in Fig. 2. For all materials, magnetic Bragg peaks are observed at 300 K, indicating long-range magnetic order. For all three compounds, the magnetic Bragg peaks are indexed by a magnetic propagation vector $\boldsymbol{k} = (\frac{1}{2}\frac{1}{2}0)$. The fitted magnetic structures are illustrated in Fig. 2. The spin structures of these materials have been previously reported and our results are generally in agreement with the existing literature [22,23]. For instance, all materials have magnetic moments that are antiferromagnetically coupled within each plane and the moments are lying within the basal plane. This result is imposed by the selected magnetic symmetries; however, allowing for lower symmetry solutions with a c-axis component did not provide an appreciative c-axis moment or improvement in quality factors. Furthermore, Mössbauer spectroscopy is also consistent with moments lying within the basal plane.

For the single-layer materials Sr_2FeO_3Cl and Ca_2FeO_3Cl, our fitted spin structures are entirely consistent with the literature [23]. The magnetic space group is P_C-42_1m (# 113.273) in BNS notation in the standard setting. This is a maximal magnetic space group of the parent nonmagnetic $P4/nmm$ space group. The allowed moments are $(m_x, m_x, 0)$, so the spins are constrained by symmetry to the basal plane. Interestingly, at 300 K there is still some diffuse scattering present at the magnetic Bragg peak locations. This is most notable for Sr_2FeO_3Cl with $T_N \approx$ ~~310~~ K, and thus this may relate to the strong quasi-2D nature of the magnetism coupled with a small width to the transition caused by minor defect concentrations. Based on the literature for this family of materials [19,33], we

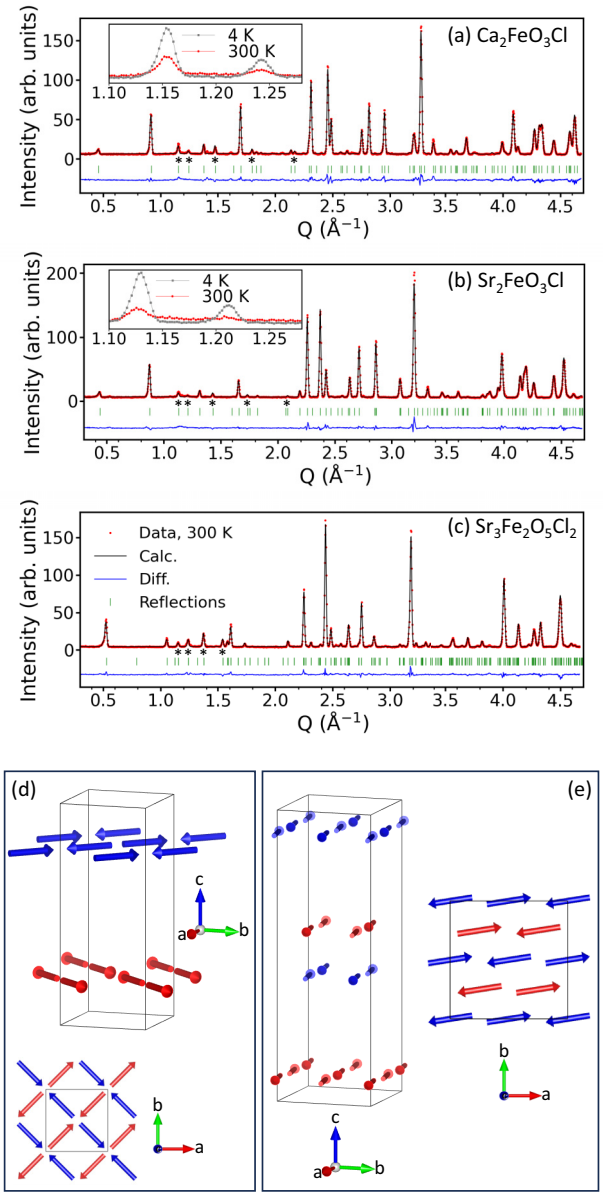

FIG. 2. Neutron diffraction data at 300 K for (a) Ca_2FeO_3Cl, (b) Sr_2FeO_3Cl, and (c) $Sr_3Fe_2O_5Cl_2$. The insets in (a) and (b) highlight diffuse scattering present at 300 K by comparison to data at $T = 4$ K. For all datasets, the magnetic propagation vector is $\boldsymbol{k} = (\frac{1}{2}, \frac{1}{2}, 0)$. The refinements shown were performed using magnetic space groups that include the propagation vector to transform the unit cell size, and hence only require one set of reflection marks. Prominent magnetic reflections are marked with a "*". Magnetic structures found in (d) Sr_2FeO_3Cl and Ca_2FeO_3Cl, and (e) $Sr_3Fe_2O_5Cl_2$. Moments are colored in red or blue depending on their z coordinate to aid in viewing along [001]. Each layer is compensated within the Néel or G-type antiferromagnetic structures. The grey box indicates the magnetic unit cell.

expect that either oxidation (replacing Cl by O) or reduction (O or Cl vacancies, excess Cl) would result in a reduction of T_N relative to that in an ideal Sr_2FeO_3Cl or $Sr_3Fe_2O_5Cl_2$ crystal where only Fe^{3+} is present. For instance, $Sr_3Fe_2O_5Cl_2$ can be reduced to $Sr_3Fe_2O_4Cl_2$ and the result is a network of Fe^{2+} that order below $T_N = 378(10)$ K [33].

For $Sr_3Fe_2O_5Cl_2$, the magnetic structure we use is equivalent to the literature, although we report it in a standard setting and find a small difference in the spin angle. The antiferromagnetic order is G-type where the moment on each Fe is aligned antiparallel to all five neighboring moments. The magnetic space group, however, is not a maximal space group since those only allow equal moments in the a and b directions, or moments solely along the c axis. These constraints do not fit the data. Instead, the symmetry has to be lowered further to allow different values of the moment in the a and b directions. This implies a symmetry breaking from tetragonal to monoclinic or lower. This was noted by Knee *et al.* [22] and they reported a possible space group as $B112/m$, which is a subgroup of $I4/mmm$. Our analysis agrees with this and could not find a higher symmetry magnetic space group compatible with the data. The magnetic space group was determined to be C_c2/m (# 12.63) with different a and b moments allowed, but with no c-axis component allowed in this space group. The orientation of the moments are free to rotate within the basal plane and Knee *et al.* reported a 6° rotation of the moments away from [100] in $Sr_3Fe_2O_5Cl_2$ (reported as 39° from [110] owing to the setting of the magnetic space group) [22]. Our refinements yield a 9.1(8) degree tilt away from [100]. Further inspection of what drives this orientation and any consequences of this symmetry is warranted.

The data in Fig. 2 confirm magnetic order at 300 K and the corresponding fitted moments are 2.2889(10) μ_B/Fe for Ca_2FeO_3Cl, 1.81(2) μ_B/Fe for Sr_2FeO_3Cl, and 3.09(3) for $Sr_3Fe_2O_5Cl_2$. At $T = 4$ K, the fitted moments are 3.890(17) μ_B/Fe for Ca_2FeO_3Cl and 3.929(14) μ_B/Fe for Sr_2FeO_3Cl; data for $Sr_3Fe_2O_5Cl_2$ were not collected at 4 K. Additional results from these refinements are provided within the SM [30].

B. Mössbauer spectroscopy

~~Because of the high ordering temperatures and quasi-2D nature,~~ ~~the~~ Néel temperatures of these materials are difficult to ascertain from magnetization measurements alone. Thus, we utilized Mössbauer spectroscopy to establish the Néel temperatures of Sr_2FeO_3Cl, Ca_2FeO_3Cl, and $Sr_3Fe_2O_5Cl_2$. Mössbauer spectra at select temperatures are plotted in Figs. 3(a)–3(c) and the results from fitting the spectra are shown in Figs. 3(d) and 3(e). Measurements were performed on powders synthesized via solid state reactions. The isothermal measurements were made sequentially upon warming the sample until a paramagnetic spectrum was observed. In the paramagnetic state, a simple doublet is observed and fitted to a single component, consistent with the crystallographic unit cell. This yields the quadrupole splitting (ΔE_Q), which was found to be relatively constant across all temperatures as shown within the SM [30].

Upon cooling below T_N, the spectrum for each compound splits into a sextet and the splitting, which is proportional to the hyperfine field (H_{hf}) increases upon cooling. The temperature dependence of the hyperfine field is quite similar in the different compositions, as demonstrated in Fig. 3(d) where the normalized hyperfine field is plotted versus the relative

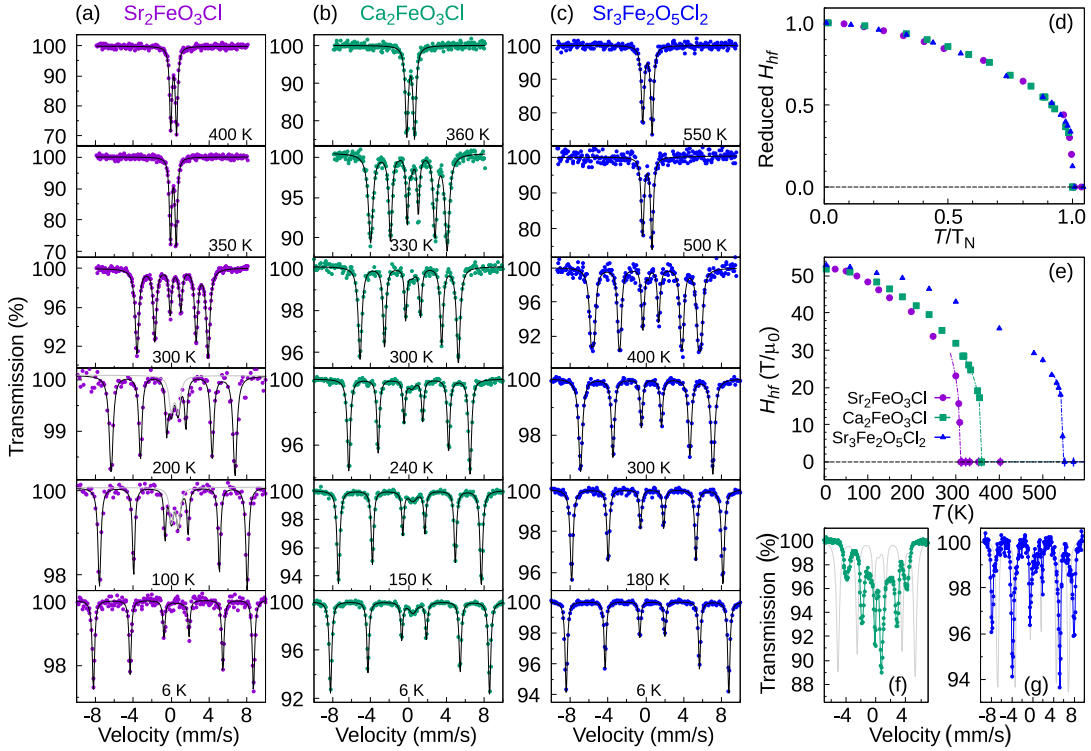

FIG. 3. Mössbauer spectra for (a) Sr_2FeO_3Cl, (b) Ca_2FeO_3Cl, and (c) $Sr_3Fe_2O_5Cl_2$ with data and total fits (black lines) shown at select temperatures. (d) A universal temperature dependence of the hyperfine field is observed across these three materials. This panel shares a legend with panel (e), which shows H_{hf} vs temperature with fits (solid lines) utilized to obtain the T_N values. (f) Comparison of spectra at ≈300 K for single crystal Ca_2FeO_3Cl (markers) and fitted result (line) of the polycrystalline sample, and (g) comparison of spectra at ≈300 K for single crystal $Sr_3Fe_2O_5Cl_2$ (markers) and the fitted result (line) of the polycrystalline sample.

temperature. The spectra were fit using a single magnetic component (an impurity component with paramagnetic nature is also fitted in the case of Sr_2FeO_3Cl and Ca_2FeO_3Cl) at base temperature; upon increasing temperature to above 1/3 of T_N more sextets are needed, as the lines broaden out a bit. All the sextets exhibited the same quadrupole splitting. The most likely origin of the broadening is a distribution of T_N related to defects.

Fitting the Mössbauer spectra yields the isomer shift (δ), ΔE_Q, and the average H_{hf} as a function of temperature. The Néel temperatures are obtained by fitting the temperature-dependent hyperfine field data as shown in Fig. 3(e). The Néel temperatures of Sr_2FeO_3Cl and Ca_2FeO_3Cl are similar; Sr_2FeO_3Cl has $T_N \approx 311$ K and orders at lower T than Ca_2FeO_3Cl with $T_N \approx 360$ K. The difference is presumably caused by the smaller lattice parameters for Ca_2FeO_3Cl compared to Sr_2FeO_3Cl though the relative importance of in-plane and out-of-plane interactions is unclear. The double-layer compound $Sr_3Fe_2O_5Cl_2$ orders significantly higher, with $T_N \approx 545$ K obtained for the polycrystalline sample. The hyperfine fields saturate to slightly greater than 50 T in all three phases. In $Sr_3Fe_2O_5Cl_2$, the hyperfine field is already larger than 40 T at room temperature. Similar H_{hf} has been previously reported for $Sr_3Fe_2O_5Cl_2$, $Sr_3Fe_2O_6$, and Sr_2FeO_3Cl [19,21,34].

The fitting procedure also reveals information about the magnetic anisotropy. The analysis indicates that the hyperfine field and the principal axis of the electric field gradient V_{zz} are perpendicular in these materials. Considering the site symmetry for iron, with a fourfold axis along [001], this indicates that the ordered iron magnetic moments are in the *ab* plane. This result is in agreement with the previous Mössbauer spectroscopy analysis performed on single crystalline $Sr_3Fe_2O_5Cl_2$ [21]. These results complement the neutron diffraction data, which also point to easy-plane magnetization.

Upon heating, some broadening of the spectra is observed, which is indicative of an increasing width of the hyperfine field distribution. Furthermore, below T_N, an additional paramagnetic component is observed in the data for Sr_2FeO_3Cl and Ca_2FeO_3Cl. Paramagnetic contributions below the apparent T_N values may come from grains with significant defects or other secondary phases.

In addition to these results on polycrystalline samples, we performed measurements on single crystals of $Sr_3Fe_2O_5Cl_2$ and Ca_2FeO_3Cl at room temperature. The spectra for the crystals are compared to the spectra for the polycrystalline samples in Fig. 3(f) for Ca_2FeO_3Cl and Fig. 3(g) for $Sr_3Fe_2O_5Cl_2$; the results for the polycrystalline samples are represented by their fitted curves that are shown as thin grey lines. Visual inspection of the data reveals a smaller splitting of the spectra for the Ca_2FeO_3Cl crystal compared to the powder, whereas a larger splitting is observed for the $Sr_3Fe_2O_5Cl_2$ crystal relative to the corresponding powder. Given that the hyperfine field evolves smoothly upon cooling

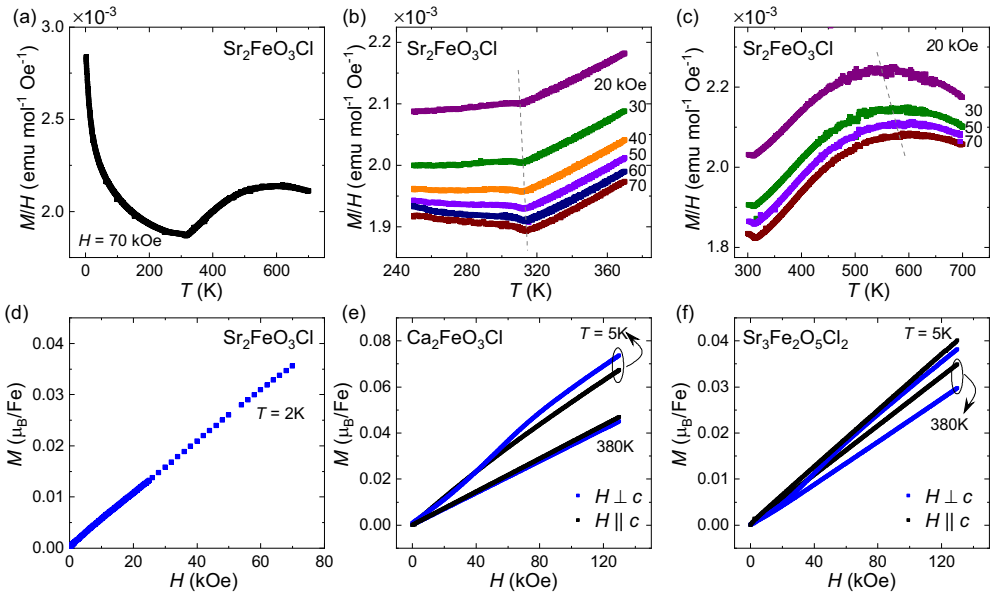

FIG. 4. Plots in the upper row in (a)–(c) contain temperature-dependent magnetization data for polycrystalline Sr_2FeO_3Cl. (a) High-field $M(T)$ data revealing a kink near T_N and broad maximum at more than $2T_N$ indicative of short-range (2D) order above T_N. (b),(c) Evolution of kink near T_N and broad maximum at high T as a function of the applied field. The lower row shows the isothermal magnetization data for (d) polycrystalline Sr_2FeO_3Cl, (e) single crystalline Ca_2FeO_3Cl, and (f) single crystalline $Sr_3Fe_2O_5Cl_2$.

from T_N, as observed in Fig. 3(d), a larger hyperfine field implies a higher ordering temperature. From this, we thus speculate that the single crystalline $Sr_3Fe_2O_5Cl_2$ has a higher ordering temperature than our current polycrystalline analog, while the crystal of Ca_2FeO_3Cl seems to order at a lower temperature than our polycrystalline sample. These results point to the need for an investigation into the roles of defects and show that Mössbauer spectroscopy is an important tool for probing these materials. Complementary local probes of the magnetism and crystal chemistry may be necessary for understanding why samples produced in different manners possess different T_N, and such an investigation into the impact of synthesis is beyond the scope of this paper. Recall again that the powders are not obtained by grinding the crystals but rather through a solid state synthesis approach. To more quantitatively compare the crystals and powders, the spectra were fit as originally discussed for the powders. Fitting the spectra yields average fields for the ordered part of the spectra of $H_{hf} = 24.4\,\mathrm{T}$ for single crystalline Ca_2FeO_3Cl and $H_{hf} = 46.6\,\mathrm{T}$ for single crystalline $Sr_3Fe_2O_5Cl_2$. We do not believe these differences observed between single crystals and polycrystalline materials are caused by thermal uncertainties but further direct comparisons are necessary to understand the results.

C. Magnetization

As established by the Mössbauer spectroscopy and neutron diffraction data in our paper and in previous studies [21,22,34], these Fe-based oxychlorides have high-spin ($S = 5/2$) moments that order at high temperatures. As such, we expect small induced magnetization (M) and low magnetic susceptibility ($\chi = M/H$). One consequence of this is that defects or small concentrations of impurities can impact the magnetization signal. In addition, the crystal structures are characterized by isolation of the magnetic sublattices and thus the magnetism is expected to be quasi-2D, implying that there is likely to be significant short range (2D) order above the Néel temperatures. Taken together, these characteristics lead to magnetic systems that are difficult to probe with magnetization measurements. We thus emphasize results for Sr_2FeO_3Cl since it has the lowest T_N that is most accessible.

The temperature-dependent magnetization data for polycrystalline Sr_2FeO_3Cl are shown in Fig. 4(a). Overall, the magnitude of the magnetization does not change much with temperature due to the strong AFM coupling of the spins below and above T_N. A kink (minimum) at approximately 310 K is associated with the Néel temperature. The temperature of this feature in $M(T)$ is in very good agreement with the Mössbauer spectroscopy data for this composition. At much higher T, a broad maximum is observed in $M(T)$ due to short-range order associated with the quasi-2D nature of the magnetism and the very strong interaction energies. This demonstrates that very high temperatures would be required to recover Curie-Weiss behavior in these materials. The kink at T_N and the broad maximum shift to slightly higher T with increasing applied field, as illustrated in Figs. 4(b) and 4(c), respectively. While the change is small, the trend is opposite what one would expect for antiferromagnets that are compensated within each magnetic layer as evidenced by neutron diffraction; quasi-2D antiferromagnets with A-type order may respond differently to the applied field since the short-range (2D) order would be ferromagnetic in nature. Our limited neutron diffraction data do not detect any major changes in the magnetic structure between 300 and 4 K, and the diffraction data and Mössbauer spectroscopy together point toward easy-

plane magnetism. Thus, the origin for the field dependence of the kink and broad maximum is unclear and work on single crystalline samples may prove valuable in understanding this behavior.

The net magnetization in these samples is indeed quite low. For Sr_2FeO_3Cl, an applied field of 70 kOe induces ≈0.035 μ_B/Fe at $T = 2$ K, as illustrated in Fig. 4(d). As noted, this value does not change significantly with temperature. Considering this, it is apparent that the overall magnetization is well compensated in the antiferromagnetic order. As a result of this small magnetization, defect spins can impact the magnetization data. Indeed, the rise in M upon cooling looks dramatic in Fig. 4(a), but the absolute scale of the axis is zoomed-in owing to the weak temperature dependence caused by the significant short-range order above T_N that decreases the susceptibility even at high T. The rise upon cooling likely relates to defect spins causing a paramagnetic contribution (a Curie tail).

Isothermal magnetization data are shown in Figs. 4(e) and 4(f) for single crystals of Ca_2FeO_3Cl and $Sr_3Fe_2O_5Cl_2$. At $T = 380$ K, the $M(H)$ curves are both nearly linear and there is only a small orientation dependence. At $T = 5$ K, a weak anomaly or nonlinearity is observed near 40 kOe for $H \perp c$; the data are plotted as M/H versus H within the SM [30] for a complementary perspective on the behavior. The applied field does not have a significant influence due to the large ordering temperatures (strong magnetic interactions). We were surprised that a larger anisotropy does not exist; given the easy-plane magnetism one expects M/H to be larger for $H||[001]$ than for $H \perp c$. The small anisotropy is likely related to the strong magnetic interactions in the system. Higher field measurements may prove insightful.

D. Optical spectroscopy

The optical absorption spectra of Ca_2FeO_3Cl, $Ca_3Fe_2O_5Cl_2$, and $Sr_3Fe_2O_5Cl_2$ are presented in Fig. 5. The general absorption features are similar between all three materials. They exhibit minimal absorption below 2 eV, a series of subtle absorption peaks near 2.5, 2.9, and 3.4 eV, and a maximum in absorption occurring between 4 and 4.7 eV. The lack of absorption below 2 eV indicates a semiconducting gap. While the overall features are similar, the peak near 2.9 eV is more prominent in the bilayer compounds than the single layer Ca_2FeO_3Cl and the opposite is true for the peak near 3.4 eV.

To determine if the apical chlorine ion has a significant impact on the optical band gap, we compare the absorption data of these oxychlorides to brownmillerite $SrFeO_{2.5}$ and perovskite $SrFeO_2F$, which also possess nominal Fe^{3+}. A clear red shift of the absorption edge is visible for the oxychlorides compared to the oxide and oxyfluoride. The band gaps of $SrFeO_{2.5}$ and perovskite $SrFeO_2F$ are approximately 2.3–2.5 eV [35–37], roughly 0.2–0.3 eV larger than in the oxychlorides. Similarly, $LaFeO_3$ has a gap of ≈2.34 eV [38]. The Ruddlesden-Popper $LaSrFeO_4$ phase does not have appreciable optical absorption below 2.3 eV [39], indicating that the layered structure found in the oxychlorides is unlikely to be responsible for the red shift present in oxychlorides compared to oxides. Instead, we attribute the band gap reduction to the lesser electronegativity of the Cl anions compared to O and F. In heteroanionic perovskite-based materials, the valence band states contain significant contributions from the anion-derived p orbitals [40]. We speculate that the increased covalency within the oxychlorides leads to an increase in the valence band maximum position, thus reducing the band gap, similar to electronic structure trends found in oxynitrides compared to oxides [41]. One source for a caveat to this discussion is the displacement of oxygen away from the apical Cl of the FeO_5Cl octahedra in the oxychlorides. First principles calculations probing the electronic distribution in the FeO_5Cl units would be useful for understanding the importance of this distortion as it relates to the band gap and the magnetic anisotropy.

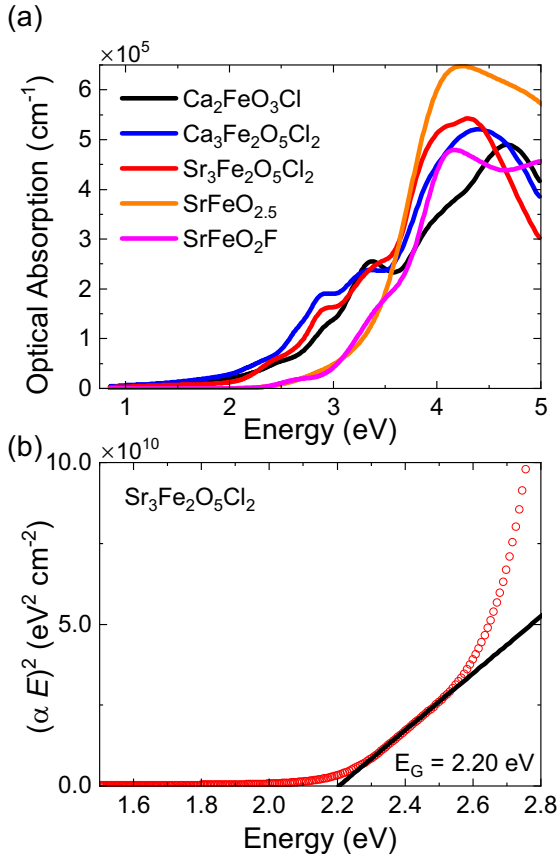

FIG. 5. (a) Optical absorption data obtained from oxychlorides, oxides, and oxyfluorides, all of which contain Fe in a nominal 3+ oxidation state. The $SrFeO_{2.5}$ and $SrFeO_2F$ materials are epitaxial films (≈25-nm thick) reported on in Ref. [35]. (b) Tauc analysis for $Sr_3Fe_2O_5Cl_2$; additional fits are in the SM [30].

To quantify the band gaps, we analyzed the optical absorption data using a direct gap Tauc model [42]. The analysis for $Sr_3Fe_2O_5Cl_2$ is shown in Fig. 5(b) as an example and the remaining fits are shown within the SM [30]. The Tauc analysis utilizes a plot of $(\alpha E)^2$ as a function of photon energy (E) and the band gap is obtained from the x-axis intercept of a linear fit as shown. While commonly used, a central challenge with Tauc analysis is determining the appropriate energy range to apply the linear fit. To minimize subjectivity, we take the derivative of $(\alpha E)^2$ with respect to E and then utilized

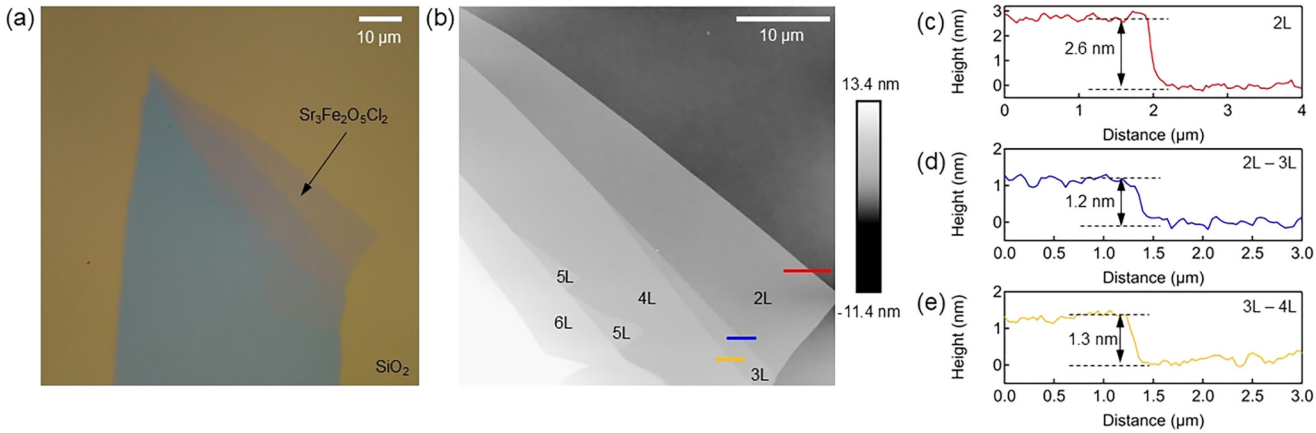

FIG. 6. Demonstration of exfoliation to ultrathin limit starting with a bulk $Sr_3Fe_2O_5Cl_2$ crystal. (a) Optical microscope image of exfoliated flake showing contrast similar to that of exfoliated BN. (b) Atomic force microscope topography image with number of layers (L) indicated. (c)–(e) AFM line scans over step edges indicated by the thick lines of like colors drawn on the image in (b).

the energy range that is ±0.1 eV of the lowest-energy local maxima in the derivative curve. This ensures we are analyzing the data where the absorption rapidly increases due to the lowest energy absorption edge. The obtained optical gaps are 2.19 eV, 2.08 eV, and 2.20 eV for Ca_2FeO_3Cl, $Ca_3Fe_2O_5Cl_2$, and $Sr_3Fe_2O_5Cl_2$, respectively.

Alternative methods for band-gap determination were also implemented but did not yield results that were consistent with the measured absorption spectrum. As an example, Fig. S3 within the SM [30] shows a linear fit to the absorption data for Ca_2FeO_3Cl using the same methodology as the direct gap Tauc analysis. The obtained x axis intercept is 1.90 eV when fitting just the absorption data. As can be seen in the absorption spectrum for Ca_2FeO_3Cl plotted in Fig. 5(a), the gap value obtained from the direct gap Tauc model (2.19 eV) is consistent with an upturn in the absorption, which is not present at 1.90 eV. We also attempted to fit the data using an indirect gap Tauc analysis. This produced optical gaps of 1.4–1.8 eV, which are not consistent with the absorption onsets observed in the data. Therefore, we conclude that the direct gap Tauc method is the most appropriate approach for extracting band gaps from the measured absorption spectra in these materials.

E. Exfoliation

Next, we present preliminary results for the mechanical exfoliation of $Sr_3Fe_2O_5Cl_2$. Scotch tape exfoliation was performed inside a glovebox filled with argon. An optical image of an exfoliated crystal is shown in Fig. 6(a). The cleavability and optical contrast of these oxychlorides are fairly similar to that of other antiferromagnetic vdW layered materials with similar bandgaps, such as $FePS_3$ [43]. Atomic force microscopy (AFM) inside the inert gas environment was utilized to investigate the flake thickness and roughness with a topography map shown in Fig. 6(b). AFM measurements demonstrate atomically flat terraces with uniform thicknesses. Line scans across various step edges are shown in Figs. 6(c)–6(e). The thinnest region of this flake has a thickness of one unit cell. The monolayer' limit of $Sr_3Fe_2O_5Cl_2$ would have a thickness of $\approx c/2$ since there are two covalently bound layers per unit cell (two vdW gaps per unit cell). The observed step edges of 1.2 nm and 1.3 nm in Figs. 6(d) and 6(e) are consistent with the expected thickness of $\approx c/2$ for single-layer steps. Additional AFM images of exfoliated flakes are shown within the SM [30]. Similar exfoliation behavior is anticipated for Sr_2FeO_3Cl and Ca_2FeO_3Cl and related oxychlorides since the van der Waals gaps in these materials originate from similar bonding motifs. Indeed, these materials are identified as having moderately low binding energies in the Materials Cloud 2D crystals database (MC2D) [44,45].

Work is underway to probe the magnetic behavior of exfoliated flakes. One challenge for such studies in the 2D limit is the nature of the magnetic structure since many probes are sensitive to moments pointing out of the plane, opposite to the magnetic anisotropy of these materials. Additionally, over a period of roughly two years, bulk crystals stored in air grew darker, suggesting a slow oxidation or uptake of water from the air. Ultrathin crystal flakes should be assumed to be air sensitive until determined otherwise and studies directed at the stability of thin flakes are needed. This study thus motivates more detailed investigations of exfoliated flakes and the ability to manipulate magnetism in the bulk phases.

IV. CONCLUSIONS

A set of complementary measurements was performed on polycrystalline samples and single crystals of Fe-based oxychlorides to assess their magnetic, optical, and mechanical behaviors. Our measurements confirmed prior results regarding the magnetic structures and high magnetic ordering temperatures, and revealed that the optical gaps are roughly 2.1(1) eV. Initial exfoliation experiments on $Sr_3Fe_2O_5Cl_2$ demonstrate behavior comparable to that of vdW materials like $FePS_3$, with a flake thickness of a single unit cell being achieved by mechanical exfoliation. With bulk ordering temperatures approaching 600 K, the double-layer compounds $Ca_3Fe_2O_5Cl_2$ and $Sr_3Fe_2O_5Cl_2$ will likely enable long-range magnetic order at ambient conditions to be obtained in crystals exfoliated to thicknesses of 1–2 nm. As such, these materials may prove to be important platforms for developing next-generation information devices. We hope this paper motivates

further studies into controlling the magnetism, the roles of defects, and the stability and functionality of exfoliated flakes.

ACKNOWLEDGMENTS

This work was supported by the U. S. Department of Energy, Office of Science, Basic Energy Sciences, Materials Sciences and Engineering Division. This research used resources at the High Flux Isotope Reactor, a U.S. DOE Office of Science User Facility operated by the Oak Ridge National Laboratory. The beam time was allocated to HB-2A (POWDER) on Proposal No. IPTS-29118. Exfoliation efforts (D.O., X.X.) were supported by Air Force Office of Scientific Research (AFOSR) Multidisciplinary University Research Initiative (MURI) program, Grant No. FA9550- 19-1-0390. Atomic force microscopy analysis (DO) was supported by the U.S. Department of Energy, Office of Science, Basic Energy Sciences, EPSCoR, and Materials Sciences and Engineering Division under Award No. DE-SC0025319. Optical measurements (B.M.L. and S.J.M.) were supported by the National Science Foundation, under Grant No. CMMI-2001888. We are grateful to R. Synowicki for assistance with ellipsometry measurements from the $SrFeO_{2.5}$ and $SrFeO_2F$ films. We thank M. Gibertini for useful discussions regarding the Materials Cloud 2D crystals database. Finally, we thank A. Christianson and J. Yan for useful discussions.

DATA AVAILABILITY

The data that support the findings of this article are openly available [31].

[1] K. S. Novoselov, D. Jiang, F. Schedin, T. Booth, V. Khotkevich, S. Morozov, and A. K. Geim, Two-dimensional atomic crystals, Proc. Natl. Acad. Sci. USA **102**, 10451 (2005).

[2] E. Suárez Morell, J. D. Correa, P. Vargas, M. Pacheco, and Z. Barticevic, Flat bands in slightly twisted bilayer graphene: Tight-binding calculations, Phys. Rev. B **82**, 121407(R) (2010).

[3] R. Bistritzer and A. H. MacDonald, Moiré bands in twisted double-layer graphene, Proc. Natl. Acad. Sci. USA **108**, 12233 (2011).

[4] H. Zeng, J. Dai, W. Yao, D. Xiao, and X. Cui, Valley polarization in MoS_2 monolayers by optical pumping, Nat. Nanotechnol. **7**, 490 (2012).

[5] D. Xiao, G.-B. Liu, W. Feng, X. Xu, and W. Yao, Coupled spin and valley physics in monolayers of MoS_2 and other group-VI dichalcogenides, Phys. Rev. Lett. **108**, 196802 (2012).

[6] J. R. Schaibley, H. Yu, G. Clark, P. Rivera, J. S. Ross, K. L. Seyler, W. Yao, and X. Xu, Valleytronics in 2D materials, Nat. Rev. Mater. **1**, 16055 (2016).

[7] Y. Cao, V. Fatemi, S. Fang, K. Watanabe, T. Taniguchi, E. Kaxiras, and P. Jarillo-Herrero, Unconventional superconductivity in magic-angle graphene superlattices, Nature (London) **556**, 43 (2018).

[8] L. Wang, E.-M. Shih, A. Ghiotto, L. Xian, D. A. Rhodes, C. Tan, M. Claassen, D. M. Kennes, Y. Bai, B. Kim *et al.*, Correlated electronic phases in twisted bilayer transition metal dichalcogenides, Nat. Mater. **19**, 861 (2020).

[9] B. Huang, M. A. McGuire, A. F. May, D. Xiao, P. Jarillo-Herrero, and X. Xu, Emergent phenomena and proximity effects in two-dimensional magnets and heterostructures, Nat. Mater. **19**, 1276 (2020).

[10] P. V. Pham, S. C. Bodepudi, K. Shehzad, Y. Liu, Y. Xu, B. Yu, and X. Duan, 2D heterostructures for ubiquitous electronics and optoelectronics: Principles, opportunities, and challenges, Chem. Rev. **122**, 6514 (2022).

[11] B. Flebus, D. Grundler, B. Rana, Y. Otani, I. Barsukov, A. Barman, G. Gubbiotti, P. Landeros, J. Akerman, U. S. Ebels *et al.*, The 2024 magnonics roadmap, J. Phys.: Condens. Matter **36**, 363501 (2024).

[12] B. Zhang, P. Lu, R. Tabrizian, P. X.-L. Feng, and Y. Wu, 2D magnetic heterostructures: Spintronics and quantum future, npj Spintronics **2**, 6 (2024).

[13] V. Baltz, A. Manchon, M. Tsoi, T. Moriyama, T. Ono, and Y. Tserkovnyak, Antiferromagnetic spintronics, Rev. Mod. Phys. **90**, 015005 (2018).

[14] T. Jungwirth, X. Marti, P. Wadley, and J. Wunderlich, Antiferromagnetic spintronics, Nat. Nanotechnol. **11**, 231 (2016).

[15] D. Xiong, Y. Jiang, K. Shi, A. Du, Y. Yao, Z. Guo, D. Zhu, K. Cao, S. Peng, W. Cai *et al.*, Antiferromagnetic spintronics: An overview and outlook, Fundam. Res. **2**, 522 (2022).

[16] A. Dal Din, O. Amin, P. Wadley, and K. Edmonds, Antiferromagnetic spintronics and beyond, npj Spintronics **2**, 25 (2024).

[17] S. E. Dann, M. T. Weller, D. B. Currie, M. F. Thomas, and A. D. Al-Rawwas, Structure and magnetic properties of Sr_2FeO_4 and $Sr_3Fe_2O_7$ studied by powder neutron diffraction and Mössbauer spectroscopy, J. Mater. Chem. **3**, 1231 (1993).

[18] D. C. Peets, J.-H. Kim, P. Dosanjh, M. Reehuis, A. Maljuk, N. Aliouane, C. Ulrich, and B. Keimer, Magnetic phase diagram of $Sr_3Fe_2O_{7-\delta}$, Phys. Rev. B **87**, 214410 (2013).

[19] P. Gallagher, J. MacChesney, and D. Buchanan, Mössbauer effect in the system $Sr_3Fe_2O_{6-7}$, J. Chem. Phys. **45**, 2466 (1966).

[20] W. Leib and H. Müller-Buschbaum, Ein neues oxohalogenoferrat: $Sr_3Fe_2O_5Cl_2$, Z. Anorg. Allg. Chem. **518**, 115 (1984).

[21] J. F. Ackerman, The preparation and structures of the alkaline earth iron oxyhalides, J. Solid State Chem. **92**, 496 (1991).

[22] C. S. Knee, M. A. Field, and M. T. Weller, Neutron diffraction study of the antiferromagnetic oxyhalides $Sr_3Fe_2O_5Cl_2$, $Sr_3Fe_2O_5Br_2$ and $Sr_3FeCoO_5Cl_2$, Solid State Sci. **6**, 443 (2004).

[23] A. L. Hector, C. S. Knee, A. I. MacDonald, D. J. Price, and M. T. Weller, An unusual magnetic structure in Sr_2FeO_3F and magnetic structures of K_2NiF_4-type iron(iii) oxides and oxide halides, including the cobalt substituted series $Sr_2Fe_{1-x}Co_xO_3Cl$, J. Mater. Chem. **15**, 3093 (2005).

[24] W. Leib and H. Müller-Buschbaum, Ein neuer bautyp der oxohalogenoferrate: $Ba_3Fe_2O_5Cl_2$ und $Ba_3Fe_2O_5Br_2$, Z. Anorg. Allg. Chem. **521**, 51 (1985).

[25] N. Abe, S. Shiozawa, K. Matsuura, H. Sagayama, A. Nakao, T. Ohhara, Y. Tokunaga, and T. Arima, Magnetically induced electric polarization in $Ba_3Fe_2O_5Cl_2$ with tunable direction in three dimensions, Phys. Rev. B **101**, 180407(R) (2020).

[26] N. Sung, H. Gretarsson, D. Proepper, J. Porras, M. Le Tacon, A. Boris, B. Keimer, and B. Kim, Crystal growth and intrinsic magnetic behaviour of Sr_2IrO_4, Philos. Mag. **96**, 413 (2016).

[27] J. Rodríguez-Carvajal, Recent advances in magnetic structure determination by neutron powder diffraction, Phys. B: Condens. Matter **192**, 55 (1993).

[28] A. Wills, A new protocol for the determination of magnetic structures using simulated annealing and representational analysis (SARAh), Phys. B: Condens. Matter **276-278**, 680 (2000).

[29] J. Perez-Mato, S. Gallego, E. Tasci, L. Elcoro, G. de la Flor, and M. Aroyo, Symmetry-based computational tools for magnetic crystallography, Annu. Rev. Mater. Res. **45**, 217 (2015).

[30] See Supplemental Material at http://link.aps.org/supplemental/10.1103/PhysRevMaterials.xx.xxxxxx for [brief descripton].

[31] Data doi: https://doi.org/10.14461/oncat.data/2529045.

[32] Y. Tsujimoto, Y. Matsushita, N. Hayashi, K. Yamaura, and T. Uchikoshi, Anion order-to-disorder transition in layered iron oxyfluoride Sr_2FeO_3F single crystals, Cryst. Growth Des. **14**, 4278 (2014).

[33] E. Dixon and M. A. Hayward, The topotactic reduction of $Sr_3Fe_2O_5Cl_2$ - square planar Fe(II) in an extended oxyhalide, Inorg. Chem. **49**, 9649 (2010).

[34] A. L. Hector, J. A. Hutchings, R. L. Needs, M. F. Thomas, and M. T. Weller, Structural and Mössbauer study of Sr_2FeO_3X (X= F, Cl, Br) and the magnetic structure of Sr_2FeO_3F, J. Mater. Chem. **11**, 527 (2001).

[35] B. M. Lefler, T. Duchoň, G. Karapetrov, J. Wang, C. M. Schneider, and S. J. May, Reconfigurable lateral anionic heterostructures in oxide thin films via lithographically defined topochemistry, Phys. Rev. Mater. **3**, 073802 (2019).

[36] T. Katayama, A. Chikamatsu, H. Kamisaka, H. Kumigashira, and T. Hasegawa, Experimental and theoretical investigation of electronic structure of $SrFeO_{3-x}F_x$ epitaxial thin films prepared via topotactic reaction, Appl. Phys. Express **9**, 025801 (2016).

[37] V. Galakhov, E. Kurmaev, K. Kuepper, M. Neumann, J. McLeod, A. Moewes, I. Leonidov, and V. Kozhevnikov, Valence band structure and x-ray spectra of oxygen-deficient ferrites $SrFeO_x$, J. Phys. Chem. C **114**, 5154 (2010).

[38] M. D. Scafetta, A. M. Cordi, J. M. Rondinelli, and S. J. May, Band structure and optical transitions in $LaFeO_3$: Theory and experiment, J. Phys.: Condens. Matter **26**, 505502 (2014).

[39] J. Reul, L. Fels, N. Qureshi, K. Shportko, M. Braden, and M. Grüninger, Temperature-dependent optical conductivity of layered $LaSrFeO_4$, Phys. Rev. B **87**, 205142 (2013).

[40] H. Kageyama, K. Hayashi, K. Maeda, J. P. Attfield, Z. Hiroi, J. M. Rondinelli, and K. R. Poeppelmeier, Expanding frontiers in materials chemistry and physics with multiple anions, Nat. Commun. **9**, 772 (2018).

[41] R.-J. Xie and H. T. Hintzen, Optical properties of (Oxy)nitride materials: A review, J. Am. Ceram. Soc. **96**, 665 (2013).

[42] J. Tauc, Optical properties and electronic structure of amorphous Ge and Si, Mater. Res. Bull. **3**, 37 (1968).

[43] J.-U. Lee, S. Lee, J. H. Ryoo, S. Kang, T. Y. Kim, P. Kim, C.-H. Park, J.-G. Park, and H. Cheong, Ising-type magnetic ordering in atomically thin $FePS_3$, Nano Lett. **16**, 7433 (2016).

[44] N. Mounet, M. Gibertini, P. Schwaller, D. Campi, A. Merkys, A. Marrazzo, T. Sohier, I. E. Castelli, A. Cepellotti, G. Pizzi *et al.*, Two-dimensional materials from high-throughput computational exfoliation of experimentally known compounds, Nat. Nanotechnol. **13**, 246 (2018).

[45] D. Campi, N. Mounet, M. Gibertini, G. Pizzi, and N. Marzari, Expansion of the materials cloud 2D database, ACS Nano **17**, 11268 (2023).